Monte Carlo Investigation of Optical Coherence Tomography Retinal Oximetry

Siyu Chen, *Student Member, IEEE*, Ji Yi, Wenzhong Liu, *Student Member, IEEE*, Vadim Backman, and Hao F. Zhang*

***Abstract*—Optical coherence tomography (OCT) oximetry explores the possibility to measure retinal hemoglobin oxygen saturation level (sO_2). We investigated the accuracy of OCT retinal oximetry using Monte Carlo simulation in a commonly used four-layer retinal model. After we determined the appropriate number of simulated photon packets, we studied the effects of blood vessel diameter, signal sampling position, physiological sO_2 level, and the blood packing factor on the accuracy of sO_2 estimation in OCT retinal oximetry. The simulation results showed that a packing factor between 0.2 and 0.4 yields a reasonably accurate estimation of sO_2 within a 5% error tolerance, which is independent of vessel diameter and sampling position, when visible-light illumination is used in OCT. We further explored the optimal optical spectral range for OCT retinal oximetry. The simulation results suggest that visible spectral range around 560 nm is better suited than near-infrared spectral range around 800 nm for OCT oximetry to warrant accurate measurements.**

***Index Terms*—Monte Carlo simulation, optical coherent tomography, retinal oximetry.**

I. Introduction

HEMOGLOBIN oxygen saturation (sO_2) is an essential physiological parameter involved in the pathophysiology of various retinal diseases, including retinitis pigmentosa, diabetic retinopathy, and glaucoma [1]–[3]. It has been reported that aberrant retinal sO_2 is present before the onset of noticeable visual degradation and can be aggravated during the disease progression [4]. Thus, measuring retinal sO_2 can be invaluable in clinical applications as a potential biomarker for early diagnosis and prediction of several retinal diseases.

Numerous attempts have been made to achieve noninvasive label-free measurement of retinal sO_2. The most promising ones are based on the distinct optical properties of oxygenated hemoglobin (HbO_2) and deoxygenated hemoglobin (HbR) [5]. Since the two molecules have characteristic optical absorption spectra, their relative abundances can be determined optically, which, in turn, are used to estimate sO_2 [5]. The current approach being used for clinical applications is multiwavelength fundus ophthalmoscopy [6]–[8]. In this approach, multiwavelength illumination is integrated into a conventional fundus imager, offering a convenient cost-effective solution of measuring retinal sO_2 level. However, this diffusive backscattered-light-based imaging method lacks depth resolution, which leads to inaccurate sO_2 estimation under the influences of vessel size and retinal pigmentation [5], [9]–[11].

Another approach, photoacoustic ophthalmoscope (PAOM), has been proposed to measure retinal sO_2. PAOM detects laser-induced ultrasonic waves generated from the light absorption by chromophores, yielding sensitivity to spectral-dependent absorption differences between HbO_2 and HbR. The technique offers 3-D mapping of retinal vasculature and is less vulnerable to optical scattering in tissues [11], [12]. However, the PAOM requires physical contact between the ultrasonic transducer and the eye, which makes its clinical adoption challenging.

Retinal oximetry based on optical coherence tomography (OCT) was also recently explored [13]. OCT, being regarded as the "gold standard" in ophthalmic imaging, can provide 3-D imaging of both retinal structure and functions at a microscopic scale. The advantage of OCT retinal oximetry is its 3-D imaging capability, allowing spectroscopic information to be extracted from selected localized regions [14]. Using a broadband low-coherence light source, OCT signals intrinsically contain spectroscopic information from tissue and, thus, have the potential to quantify sO_2 based on the spectral differences in the optical properties of HbO_2 and HbR. Several experiments using near infrared (NIR) light OCT have been attempted, showing that artery and venous blood have a different attenuation curve within selected OCT spectra [14]–[17]. However, no quantitative sO_2 value was reported *in vivo*. Recently, several studies suggested that OCT working within visible-light spectral range could achieve improved accuracy in quantifying sO_2 *in vitro* [18], [19]. Furthermore, Robles *et al*. demonstrated sO_2 measurement in an intravital system [20], and Yi *et al*. implemented visible-light OCT to measure sO_2 in rat retina, showing a great promise for *in vivo* oximetry [13].

Although OCT oximetry has shown great potential, several uncertainties need to be thoroughly investigated for accurate sO_2 measurement before OCT retinal oximetry can be successfully translated into clinics. First, it is not clear how to extract OCT signals from the imaged retinal vessels to analyze optical absorption properties from the backscattered OCT signals. Biological tissues, including whole blood, are highly optically scattering media and will lead to multiple scattering of the OCT probing light. A photon that goes through multiple scattering may have different accumulative optical path length from its penetration depth, which leads to inaccurate localization, image blurring, and signal reduction [21].

Manuscript received October 24, 2014; revised January 14, 2015 and March 11, 2015; accepted April 15, 2015. Date of publication May 4, 2015; date of current version August 18, 2015. This work was supported in part by National Institute of Health Grants 1R01EY019951 and 1R24EY022883, and National Science Foundation Grants CBET-1055379, CBET-1066776, and DBI-1353952. J. Yi is supported in part by a postdoctoral fellowship award from the Juvenile Diabetes Research Foundation. *Asterisks indicates corresponding author*.

S. Chen, J. Yi, W. Liu, and V. Backman are with Northwestern University.

*H. F. Zhang is with the Department of Biomedical Engineering, Northwestern University, Evanston, IL 60208 USA and also with the Department of Opthamology, Northwestern University, Chicago IL 60611 USA (e-mail: hfzhang@northwestern.edu).

Color versions of one or more of the figures in this paper are available online at http://ieeexplore.ieee.org.

Digital Object Identifier 10.1109/TBME.2015.2424689

Second, it is not clear which spectral band is optimal for OCT retinal oximetry. Currently, two spectral bands of light sources (NIR and visible) have been reported for OCT oximetry. While the majority of clinical systems use NIR OCT for its deeper penetration depth and less phototoxicity, visible-light OCT has the advantage of higher axial resolution and, arguably, a better contrast between HbO_2 and HbR [5], [22], [23]. Since the molar extinction coefficients of HbO_2 and HbR behave dramatically differently in these two spectral bands, it is worthwhile to investigate which spectral region can offer better accuracy in OCT oximetry.

We adopted a Monte Carlo approach to investigate the effects of the aforementioned factors on the accuracy of OCT oximetry. Monte Carlo simulation is a statistical numeric method to identify approximated solutions of stochastic processes. This method is often used to study light-tissue interactions, where finding analytic solutions is technically challenging. Although Monte Carlo simulation does not usually track phase information of photons, the feasibility of Monte Carlo simulation of OCT was demonstrated by several groups [24]–[26]. By simulating the behavior of photon packets traveling across different layers and blood vessels in the retina, we can achieve a numerical approximation of spectrometric OCT signals.

In this paper, we first constructed our Monte Carlo simulation algorithm using a layered eye model. To investigate the accuracy of retinal OCT oximetry under physiological and pathological complexities, we varied the blood vessel diameter and OCT signal sampling position in our simulation, and compared the calculated sO_2 with the preset values. We also investigated the effect of the packing factor (a scaling coefficient taking into account the scattering changes due to the densely packed blood cells) on the sO_2 estimation accuracy. To further verify the numerical simulation results, we apply the same analysis procedure on the packing factor using *in vivo* animal experiment data. Finally, we compared the performances of OCT oximetry between NIR and visible spectral bands.

II. Methods and Materials

A. Eye Model

We used a 3-D four-layer model to mimic the posterior ocular structure in our Monte Carlo simulation. The overall geometry is shown in Fig. 1(a). The four layers include retina, retinal pigment epithelium (RPE), choroid, and sclera [27]. The respective thicknesses of these layers are 200, 10, 250, and 700 μm as reported in the literatures [see Fig. 1(b)] [11], [27]. The lateral boundary of each layer extended to infinity during the simulation. It has been shown that this simplified model is sufficient for retinal photon-tissue interaction simulation since other posterior ocular tissues (such as vitreous humor) are either relatively thin or optically transparent [11], [28].

We placed an infinitely long cylindrical blood vessel segment in the retina in parallel to the surface [see Fig. 1(a)]. The vessel diameter was varied from 40 to 160 μm to study the effect of vessel size [29]. Inside the blood vessel, we assumed that blood is optically homogeneous. The vessel wall thickness was set to

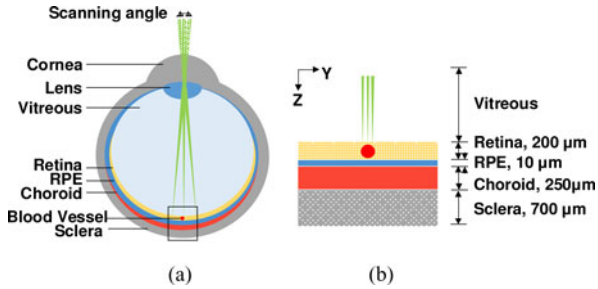

Fig. 1. Simplified eye model used in the simulation study. (a) Schematic diagram of a human eyeball. (b) Dimensions and relative positions of the layers and the blood vessel being simulated (not to scale).

TABLE I
Optical Properties of Ocular Tissue in the Monte Carlo Simulation

Wavelength range [nm]		Visible (520–610)	Near infrared (750–840)
Retina	μa [cm^{-1}]	5	1
	μs [cm^{-1}]	319	224
	g [-]	0.97	0.97
RPE	μa [cm^{-1}]	938	385
	μs [cm^{-1}]	1068	1469
	g [-]	0.84	0.84
Choroid	μa [cm^{-1}]	224	27
	μs [cm^{-1}]	711	484
	g [-]	0.94	0.94
Sclera	μa [cm^{-1}]	4	0.4
	μs [cm^{-1}]	966	614
	g [-]	0.90	0.90
Blood vessel	μa [cm^{-1}]	9	2
	μs [cm^{-1}]	284	140
	g [-]	0.84	0.84

be 10% of the lumen diameter [30]. The optical properties of solid tissues, including absorption coefficient μ_a [cm^{-1}], scattering coefficient μ_s [cm^{-1}], and anisotropy g [dimensionless], can be found in the literatures [31], [32]. We treated these optical properties as constant values inside each simulated spectrum band despite their slight wavelength dependency (see Table I). The manipulation is compatible with major oximetry algorithms to date, which do not consider the wavelength-dependent optical attenuation caused by tissues other than blood [5], [9], [13]. In addition, the optical sectioning ability of OCT allowed us to separate the backscattered signals originated from blood and other tissues. The exact way of how light propagates in deeper ocular tissues will not affect the OCT signal extracted from the blood vessels above, and thus will not affect the subsequent calculation of sO_2. However, we still modeled these layers for the completeness of the simulation.

The manipulation is also valid due to the fact that the variation in optical properties of these solid tissues are limited inside each of the simulated spectrum band (520–610 and 750–840 nm) [31], [32]. When compared with the drastic fluctuations in whole-blood optical properties, the merely 15% variations found in these non-blood retinal tissues can be neglected. We will discuss the details of absorption and scattering properties of whole blood in the next section.

B. Absorption and Scattering Properties of Whole Blood

The absorption coefficients of the whole blood within the simulated spectral ranges were calculated by [33]

$$\mu_a = 2.3 \times [\mathrm{HbT}] \times \frac{\varepsilon_{\mathrm{HbO_2}} \times \mathrm{sO_2} + \varepsilon_{\mathrm{Hb}} \times (1 - \mathrm{sO_2})}{W_{\mathrm{HbR}}} \quad (1)$$

where [HbT] [g/L] is the concentration of total hemoglobin; $\varepsilon_{\mathrm{HbO_2}}$ [$\mathrm{cm}^{-1} \cdot$ L/Mole] and $\varepsilon_{\mathrm{Hb}}$ [$\mathrm{cm}^{-1} \cdot$ L/Mole] are the molar extinction coefficient of oxyhemoglobin ($\mathrm{HbO_2}$) and HbR, respectively; $\mathrm{sO_2}$ [dimensionless] is the hemoglobin oxygen saturation, which was predefined before each simulation within the physiological range from 0.4 to 0.98 [34]; W_{HbR} is the molecular weight of the hemoglobin, which is 64 500 [g/Mole]. The absorption coefficients of fully oxygenated μ_{a_OxyB} and deoxygenated μ_{a_DeOxyB} whole blood can be obtained using a $\mathrm{sO_2}$ value of 1 and 0 in (1), respectively.

Because of the interrelationship between the optical absorption and scattering coefficients, the spectrum of scattering coefficient of the whole blood also depends on $\mathrm{sO_2}$. Using the method reported in [35], we calculated the scattering coefficients of oxygenated μ_{s_OxyB} and deoxygenated μ_{s_DeOxyB} whole blood based on Mie theory assuming that particles scatter light independently in whole blood. The results we obtained showed similar spectral shape to what was previously reported but with considerably larger values [36]–[38]. The reason is that when the erythrocytes are densely packed as in whole blood, optical scattering from blood cells are no longer independent. A scaling coefficient was needed to connect the independent and dependent scattering coefficients. We referred to this hematocrit-dependent scaling coefficient as packing factor *W* [dimensionless]. The relationship between hematocrit *H* [dimensionless] and *W* within the simulated spectral regions can be approximated using the relationship [38]

$$W = (1 - H)^2 . \quad (2)$$

Based on normal physiological value of $H = 0.45$, a packing factor $W = 0.3$ was used to scale the spectrum. Finally, the expression for the $\mathrm{sO_2}$-dependent scattering coefficient of whole blood is

$$\mu_s = W \cdot \mu_{s\_\mathrm{OxyB}} \times \mathrm{sO_2} + W \cdot \mu_{s\_\mathrm{DeOxyB}} \times (1 - \mathrm{sO_2}) . \quad (3)$$

We also derived the anisotropic factor *g* of whole blood from the Mie theory [38]. The calculated results showed that the variation of *g* was always less than 0.3% in each of the simulated spectral range, which is within the error margin of our simulation algorithm. As a result, we used the mean value of *g* within each simulated spectral band, which greatly improved the efficiency of computation. We used $g = 0.988$ for visible-light spectral range and $g = 0.982$ for NIR spectral range.

C. Monte Carlo Simulation

The Monte Carlo simulation algorithm was revised from Wang's MCML program [24]. Fig. 2 shows the flowchart of our simulation. At each optical wavelength, we first initialized the absorption and scattering coefficients of blood and ocular tissue accordingly. Then, a photon packet with unit initial weight was launched and traced. The initial propagation direction of the photon packet was set based on the current A-line location, and was scaled to a fraction of total scanning angel of $\pm 1.0°$. The path length and energy deposition of the photon packet at every scattering event site were recorded. Once a photon packet exited the tissue boundary or its weight was sufficiently small (< 0.0001) and did not survive the roulette test, the tracing was terminated [24]. To speed up the simulation, we monitored the path length of each photon packet and terminated tracing once it traveled well beyond (100 μm below the retina layer) the depth of interest. Since OCT signal is depth resolved and photon packets backscattered from deeper regions do not contribute much to the simulated OCT signals from the blood vessel, the speeding process did not affect our final results [25], [39]. Once a photon packet exited the tissue from the upper surface, we compared the exiting position and angle of emergence with its incidence position. If the photon packet falls into a collection angle of 4.2°, which equals to a numerical aperture (NA) of 0.1 for tissue with a refractive index $n = 1.38$, the weights and path length of this photon packet were recorded for OCT image construction and $\mathrm{sO_2}$ estimation. Otherwise, the photon packet was discarded (undetected) and a new iteration started. This cycle continued until we reached a stable outcome. The simulation was executed on a workstation equipped with Intel Xeon E5645 CPU at 2.40 GHz and 24 GB of memory. It took roughly 30 min to generate one A-line consisting of 4 million photons. Parallel computing technique was implemented. The generation of a single wavelength B-scan with 128 A-lines took about 10 h.

To simulate the wideband light used in OCT, we ran the simulation for multiple wavelengths. For visible spectral range, the

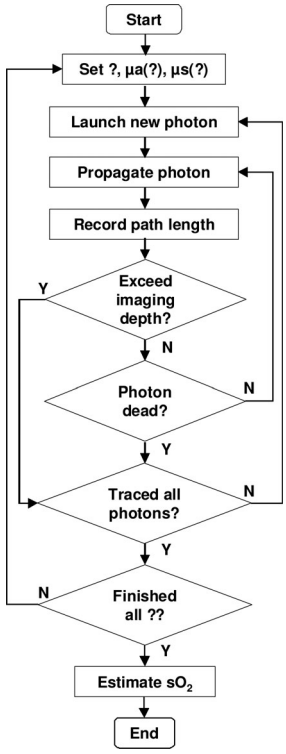

Fig. 2. Simulation flowchart of OCT oximetry.

TABLE II
OPTICAL PROPERTIES OF WHOLE BLOOD IN THE MONTE CARLO SIMULATION

λ [nm]		μ_{a_OxyB} [cm^{-1}]	μ_{a_DeOxyB} [cm^{-1}]	μ_{s_OxyB} [cm^{-1}]	μ_{s_DeOxyB} [cm^{-1}]
Visible	520	121.0	152.6	3626.3	3396.6
	525	150.7	168.1	3547.2	3339.5
	530	189.4	185.0	3459.0	3283.0
	535	224.0	201.3	3387.4	3230.1
	540	241.9	217.4	3353.1	3180.6
	545	234.0	233.0	3365.5	3136.1
	550	204.1	244.7	3407.4	3103.3
	555	174.0	249.1	3436.1	3085.9
	560	160.8	244.6	3427.1	3085.1
	565	172.9	230.3	3373.5	3097.8
	570	210.3	211.6	3289.4	3112.0
	575	244.0	193.4	3238.0	3121.5
	580	224.8	176.9	3291.1	3126.7
	585	150.7	160.6	3415.2	3132.4
	590	77.9	136.6	3504.6	3150.2
	595	36.9	104.7	3527.5	3172.7
	600	18.5	77.2	3513.4	3178.0
	605	10.8	60.6	3485.3	3163.6
	610	7.8	48.3	3452.7	3144.2
Near infrared	750	2.7	7.3	2653.2	2366.0
	755	2.9	7.9	2628.3	2341.9
	760	3.0	7.9	2603.7	2319.1
	765	3.2	7.4	2579.4	2296.9
	770	3.4	6.7	2555.3	2274.8
	775	3.5	6.1	2531.5	2252.8
	780	3.7	5.5	2508.0	2230.9
	785	3.8	5.0	2484.8	2209.1
	790	3.9	4.6	2461.8	2187.5
	795	4.1	4.2	2439.1	2166.1
	800	4.2	3.9	2416.5	2144.6
	805	4.4	3.8	2394.0	2123.2
	810	4.5	3.7	2372.1	2102.3
	815	4.6	3.6	2350.4	2081.7
	820	4.7	3.6	2328.9	2061.3
	825	4.9	3.6	2307.6	2041.1
	830	5.0	3.6	2286.6	2021.2
	835	5.2	3.6	2265.8	2001.6
	840	5.3	3.6	2245.3	1982.2

wavelength band covers from 520 to 610 nm; for NIR spectral range, the bands covers from 750 to 840 nm. We sampled the broad band spectrum at a 5 nm interval. At each sampled wavelength, the optical properties were averaged from the neighbor ± 5 nm wavelength range. The exact unscaled values of μ_{a_OxyB}, μ_{a_DeOxyB}, μ_{s_OxyB}, and μ_{s_DeOxyB} used in the simulation are summarized in Table II.

The stated process allowed us to generate the wavelength-dependent photon distribution inside the medium, analogous to OCT B-scan images.

D. Estimating sO_2 Value

In order to obtain the sO_2-dependent backscattered intensity spectrum, we sampled each simulated OCT B-scan within a rectangular region of interest (ROI). The dimensions of the ROI were 3 and 20 μm along the lateral and axial directions, respectively. We varied the depth position of the ROI within the vessel to examine the effect of sampling position on the accuracy of sO_2 estimation.

Once we obtained the spectrum, we recovered sO_2 using the following model to fit the spectrum of reflected intensity [40]:

$$I = I_0 \cdot r \cdot \exp\left(-2d \cdot \mu_{t\_\mathrm{OxyB}} \cdot \mathrm{sO}_2 - 2d \cdot \mu_{t\_\mathrm{DeOxyB}} \cdot (1 - \mathrm{sO}_2)\right) \quad (4)$$

where I_0 [arb. u.] is the intensity of incident light; d (cm) is the vessel diameter; r (dimensionless) is the reflectance from the vessel wall. The spectrum of r can be expressed by a power law $r(\lambda) = A\lambda^{-\alpha}$ under the first Born approximation, where A is a constant [41], [42]. μ_{t_OxyB} [cm^{-1}] and μ_{t_DeOxyB} [cm^{-1}] are the compound attenuation coefficients of fully oxygenated and fully deoxygenated whole blood, respectively. The compound attenuation coefficient spectrum of μ_{t_OxyB} and μ_{t_DeOxyB} were obtained as the linear combination of the absorption coefficients, scattering coefficients, and the packing factor of whole blood [43]

$$\begin{aligned} \mu_{t\_\mathrm{OxyB}} &= \mu_{a\_\mathrm{OxyB}} + W \cdot \mu_{s\_\mathrm{OxyB}} \\ \mu_{t\_\mathrm{DeOxyB}} &= \mu_{a\_\mathrm{DeOxyB}} + W \cdot \mu_{s\_\mathrm{DeOxyB}}. \end{aligned} \quad (5)$$

After applying a logarithm operation to both sides of (4) and expanding $r(\lambda)$, we have

$$\ln\left(\frac{I}{I_0}\right) = 2d\left[\mathrm{sO}_2 \cdot (-\mu_{t\_\mathrm{OxyB}} + \mu_{t\_\mathrm{DeOxyB}}) - \mu_{t\_\mathrm{DeOxyB}}\right] + \ln(\mathrm{A}) - \alpha \cdot \ln(\lambda) \quad (6)$$

which is a function of λ. Based on the notion that sO_2 cannot be less than zero or greater than one, a constrained least-squares fitting can be performed to estimate sO_2, d, ln(A), and α. The value of I was obtained by summing all photon packets' weights reflected back from the ROI. I_0 was calculated by sampling and averaging the backscattered intensity in a region immediately above the blood vessel. The dimension of the region was the same as the ROI for calculating I.

III. RESULTS

A. Stability

To verify our Monte Carlo code, we compared results from both our program and the MCML using the same eye model described above but without the embedded blood vessel. The optical properties of the tissue were selected for 610 nm. The two simulation results agreed with each other very well (data not shown). Fig. 3(a) is a whole OCT B-scan image simulated using our algorithm rendered in logarithmic scale. The layered anatomic structures of retina, RPE, and the blood vessels can be clearly identified in the simulated imaging and are identical to our eye model.

To determine the optimal number of simulated photon packets, we performed a stability test by varying the number of simulated photon packets from 0.5 to 5 million per A-line. We recorded and localized the back-scattered energy, and the mean intensity of an area $3\,\mu\mathrm{m} \times 20\,\mu\mathrm{m}$ (lateral$\times$axial) at the bottom of the blood vessel was calculated. Blood sO_2 was fixed at 70% and vessel diameter was fixed at 100 μm. We plotted the mean values and the standard deviations of the ten simulations against

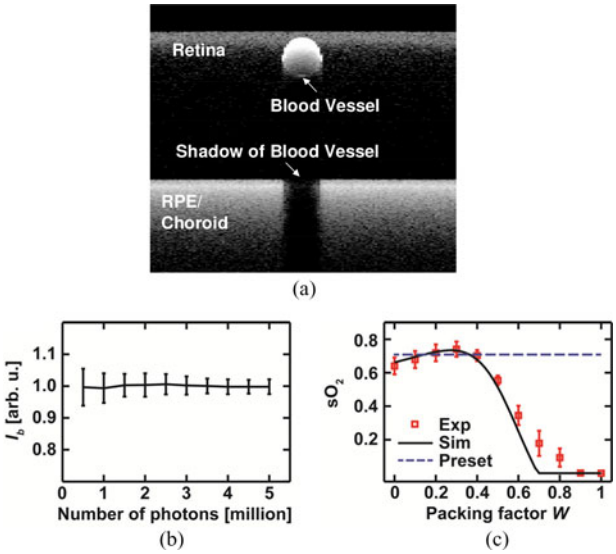

Fig. 3. (a) Sample-simulated depth-resolved broadband OCT B-scan image. (b) Stability test of backscattered OCT signal intensity I_b on different simulated photon packet numbers per scan line. (c) Estimated sO_2 value versus packing factor W range. The red box showed the real experiment result adopted from Ji *et al*. The black line is the Monte Carlo simulation result. The blue-dashed line indicates the preset sO_2 of 0.7. Exp: experimental data. Sim: data points simulated by the Monte Carlo method.

their corresponding number of photon packets in Fig. 3(b). The mean value of the reflected energy does not fluctuate with increased photon packet number. The standard deviation decreases with increased number of photon packets, which indicates the simulation gives more stable results with more simulated photon packets. When the number of photon packets exceeded four million per A-line, the standard deviation remains unchanged, indicating that we have reached a stable simulation. Based on the stability test, we chose a total photon packet number of four million per A-line, which should give us both robust simulation results and optimal simulation performance.

B. Packing Factor W

When we composed the total attenuation spectra to retrieve sO_2, the choice of an appropriate W becomes critical for accurate sO_2 estimation. Since W depends on hematocrit that varies among individuals, its true value is not always available in clinical applications. As a result, it is important to evaluate the influence of W on the accuracy of sO_2 estimation and to identify an optimal W value. After we obtained the spectra from the bottom of the blood vessel, we estimated the sO_2 values using W values from 0 to 1 with a 0.1 increment. The simulated results are shown in Fig. 3(c). As can be seen from the curve, the fitted sO_2 reaches a plateau when W is between 0.2 and 0.4 and leads to an sO_2 estimation within 5% error range from the preset value of 0.7. An underestimation of 5% to 10% can be found when we used a W value less than 0.2. The accuracy of sO_2 estimation deteriorated quickly as we increased W beyond 0.4. Within this range, significant underestimation over 20% can be found.

To verify the selected range of W, we examined sO_2 estimation using *in vivo* experimental data from rat eyes. The optical properties of rat blood were considered to be similar to that of human blood. The detailed description of the experimental procedures can be found in [13]. Briefly, we performed OCT imaging on wild-type Long Evans rat *in vivo*. The animal was anesthetized using 1.5% isoflurane mixture with oxygen/nitrogen compound gas similar to normal air. We placed the animal securely on a holder for imaging purpose. Before imaging, we applied 0.5% Tetracaine hydrochloride ophthalmic solution for local eye anesthesia and 1% Tropicamide ophthalmic solution for pupil dilation.

We used a homemade OCT system working within the visible-light spectral range. The illumination spectrum centered at 585 nm and had an 85 nm bandwidth. We acquired the three dimensional retina OCT image by raster scanning the optical illumination at 25-kHz A-line rate. The image consisted of 256 B-scans, where each B-scan had 256 A-lines. The 2-D scan covered an area of about 2 mm $\times$ 2 mm. During experiments, the inhalation gas compound was deliberately controlled and the arterial sO_2 was monitored to be exactly 0.7 by a pulse oximeter attached to the rat's rear feet. All experimental procedures were approved by the Northwestern University IACUC and conformed to the Association for Research in Vision and Ophthalmology Statement on Animal Research.

We recovered depth-resolved spectroscopic fundus image by using a series of short-time Fourier transforms [13]. We averaged the signals along the center axial of each blood vessel to improve SNR and improve estimation accuracy. Then, we extracted the backscattering spectrum in the same manner as we used in the simulation, i.e., from a rectangular ROI at the very bottom of the blood vessel manually. The spectrum was normalized by the reference spectrum. We applied the same least-squares algorithm as in simulation to extract sO_2 information in order to study the impact of empirical choice of W value from 0 to 1.

We plotted the experimental results against our simulation results in Fig. 3(c). The two results are compatible with each other. The comparison suggested that a W between 0.2 and 0.4 should be used. In addition, the choice of W should be compatible with the physiological value of blood hematocrits H, whose value normally varies from 40% (in women) to 45% (in men) in systemic circulations. Even lower values may be encountered in smaller vessels such as in the retina [44]. Combining these factors, we chose the lower value of 0.4 for H, which results a packing factor $W = 0.36$.

C. Accuracy of sO_2 Estimation

We first examined how the selected sampling ROI location affects sO_2 estimation. The first sampling position was placed at the center of the blood vessel. The second sampling position was placed near the bottom of the blood vessel, with the lower boundary of the region nearly overlapped with the posterior wall of the vessel [see Fig. 4(a)]. The same dimension was used for both sampling ROIs and the vessel diameter was fixed at 100 μm. We changed the preset sO_2 value from 0.4 to 0.98 and compared them with estimated sO_2 values from OCT oximetry. The comparison between the estimated sO_2 and

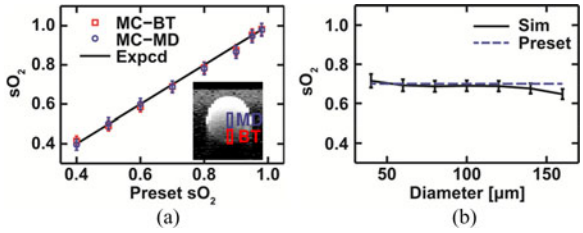

Fig. 4. (a) Influence of ROI sampling position on sO2 estimation. The ROI positions were placed near the bottom of the vessel (highlighted by red box "BT") or at the center of the vessel (highlighted by blue box "MD"). The estimated sO2 are plotted against the true value (black solid line), where the red square represents data calculated by sampling near the bottom and the blue circle for sampling at the center of the vessel, respectively. (b) Influence of vessel diameter on sO2 estimation. The preset sO2 value was 70% (blue-dashed line). The ROI sampling position was near the bottom of the vessel. Sim: data points simulated by the Monte Carlo method.

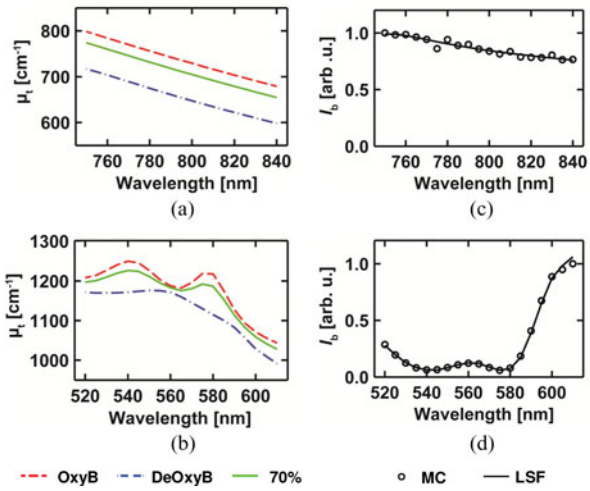

Fig. 5. Compound attenuation coefficient μ_t and Monte Carlo simulation results of NIR and visible light OCT intensities. The μ_t spectra of fully oxygenated, fully deoxygenated, and 70% oxygenated blood at NIR and visible spectral ranges are shown in (a) and (b), respectively. The spectra of normalized reflected intensities sampled at NIR and visible spectral ranges, are shown in (c) and (d), respectively. The solid line indicates the fitted curve calculated by least-square fitting.

preset sO_2 values is shown in Fig. 4(a). As the figure indicates, the estimated value and the preset value show strong positive correlation ($R^2 = 0.99$), and the deviation from the preset values is always constrained within a 5% error range. In addition, no significant difference was found between the two sampling ROI locations (BT and MD) and we selected BT ROI in the rest of our simulation.

We also evaluated the influence of blood vessel diameter on the accuracy of sO_2 estimation. Blood vessel diameter, a highly variable parameter [45] in a normal eye, can potentially affect the accuracy of OCT oximetry in a profound manner [5], [11]. Based on anatomical findings, we simulated the vessel diameter from 40 to 160 μm [29] with a 20 μm increment to investigate the influence of vessel diameter on OCT oximetry. The blood sO_2 level was set to 0.7, which is close to the physiological value of venous blood. We chose this specific value because variations in venous blood sO_2 are of greater interests to physicians. It was reported that during early pathological progress, retinal venous sO_2 showed greater changes, while arterial sO_2 remains unchanged [8], [46].

The simulation result of vessel diameter influence is shown in Fig. 4(b). No statistically significant difference was seen among the estimated sO_2 values within the simulated range of vessel diameters. However, a gradually descending trend can be observed as the vessel diameter increases. A careful examination on the simulated data revealed that the detected energy was extremely low due to higher optical absorption and scattering experienced inside the blood when vessel diameter increases. The deteriorated SNR caused underestimation in our least-squares fitting algorithm.

D. Influence From OCT Spectral Range

Currently, two spectral ranges (NIR and visible-light) were tested for OCT oximetry [13], [14], [16], [17], [19]. As both scattering and absorption properties of blood are drastically different between these two spectral bands, we carried out simulations in each band to assess their respective accuracies in sO_2 measurement.

The simulated spectral range for NIR OCT was from 750 to 840 nm, with a center wavelength at 795 nm. The selected range is slightly shorter than the spectral range currently being used in NIR OCT systems because we wanted to include the isosbestic point at 797 nm, which created maximum stability in inverse calculation of sO_2 [5], [38]. The diameter of the blood vessel was fixed at 100 μm and the sO_2 was set at 0.7. For comparison, the compound attenuation coefficient spectra of fully oxygenated blood, deoxygenated blood, and the corresponding value of whole blood at 70% sO_2 level was shown in Fig. 5(a) and (b) for the simulated NIR and visible spectral ranges, respectively. We can clearly see that the spectra of HbO_2 and HbR are almost in parallel within the NIR spectral region.

For OCT oximetry, we used $W = 0.36$ as mentioned above for both NIR and visible spectral ranges. Within the simulated NIR range, the least-squares fitting algorithm was ill-posed as the two inputs were almost linear dependent [see Fig. 5(a)]. We attempted to solve the coefficients in (6) using the same least-squares fitting algorithm as we used for the visible spectral range. But the algorithm failed to converge. The algorithm gave us infinitely many solutions that could reproduce exactly the same solid fitting curve in Fig. 5(c). As a result, converged sO_2 estimation cannot be established. On the other hand, the least-squares fitting algorithm converged nicely within the simulated visible spectral range, resulting a $sO_2 = 0.69 \pm 0.027$, as shown in Fig. 5(d).

IV. Discussion and Conclusion

In this paper, we demonstrated that OCT oximetry is able to measure blood sO_2 with a high accuracy within the simulated visible-light spectral range. The simulation results showed that the estimated sO_2 values are consistent with the predefined values varied from 0.4 to 0.98 at various vessel diameters. We also observed one exception in the simulated OCT oximetry: increasing vessel diameter causes decreased SNR and underestimation of sO_2. We believe this effect was majorly caused by the

limitation of the least-squares fitting algorithm used. A more robust fitting algorithm will enhance the estimation accuracy and avoid such situations.

In addition, we included parameter α in our least-squares fitting to compensate for the tissue (i.e., vessel wall) scattering background that is governed by the local refractive index fluctuation [42], [47]. The values of α in the various tissue types have been previously characterized to be $\sim$1 with variations around $\pm$0.2 [41]. Because α and sO_2 were independent factors in our model, the small variation of α should only had negligible effect to the sO_2 calculation.

Although the blood vessel diameter and location of ROI (i.e., inside blood vessels or at the bottom boundaries of vessels) did not seem to affect the accuracy of sO_2 estimation in our simulation, caution should be given in practical experimental setup. A proper selection of ROI position at different blood vessel diameters could greatly improve the measured backscattered intensity contrast caused by the differences in μ_{t_OxyB} and μ_{t_DeOxyB} and, thus, the accuracy of sO_2 estimation. For example, in small blood vessels, the bottom surface of the vessel provides good reflectance signal due to the refractive index mismatch between the blood and the vessel wall. The photons sampled at the bottom finished one entire round-trip inside the blood vessel, and such a double passing improves spectral contrast due to longer absorption length. In larger blood vessels, however, strong attenuation reduced photon packets survive such longer path lengths, which leads to drastic drops in signal strength and makes it more vulnerable to detection noises. To compensate for this, choosing a ROI position closer to the vessel surface within larger vessels (rather than at the bottom of the vessel) may be a good strategy for more robust inverse calculation at the cost of less absorption contrast. Taking these effects into consideration, we think that the ROI can be empirically chosen as long as it has sufficient absorption process and SNR, however, more rigorous studies could be conducted to explore whether an optimal ROI location can be identified.

Our simulation also indicates that the packing factor *W* could be chosen empirically but within the range from 0.2 to 0.4, which will yield an sO_2 estimation within a 5% error from the true value. The *W* value is compatible with the manipulation we performed to bridge the difference in scattering coefficients obtained from the Mie theory and the reported data found in the literature [38]. For *in vivo* experiments, we recommend that a *W* value should be selected after being calibrated of the estimated sO_2 in arterial blood because arterial sO_2 value can usually be acquired by a systemic oximeter. Further, the *W* value should be consistent with the physiological value of hematocrit, which can be determined through blood sampling if necessary.

Finally, we compared OCT oximetry within visible light and NIR spectral ranges. We failed to solve quantitatively for an sO_2 level using NIR light in the simulation. An examination of the fully oxygenated and fully deoxygenated blood scattering coefficients, calculated by Mie theory, indicates a parallel (dependent) relationship within the NIR spectral range from 750 to 840 nm. When we used $W = 0.3$ to scale the scattering coefficients for simulation, μ_s for oxygenated whole blood ranges from 643.3 to 770.4 cm^{-1} and μ_s for deoxygenated whole blood ranges

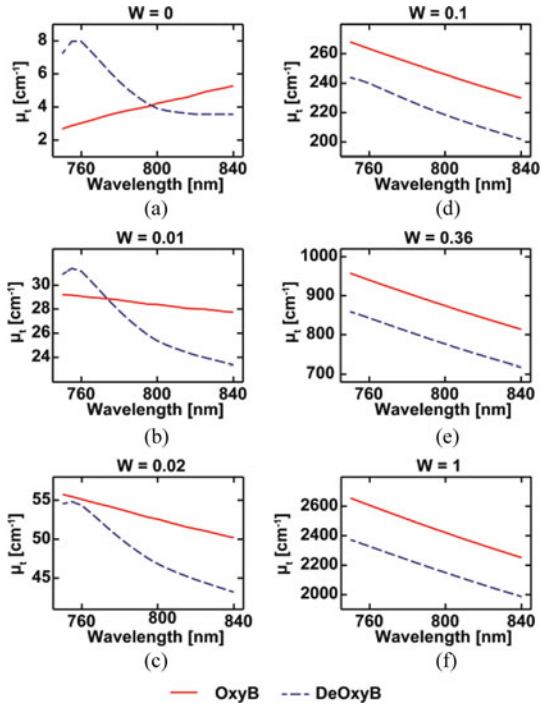

Fig. 6. Compound attenuation coefficients μ_t with respect to different packing factor W. The spectra are independently normalized. (a) to (d) are arranged based on increasing *W* values at 0, 0.01, 0.02, 0.1, 0.36, and 1.

from 563.0 to 676.2 cm^{-1}. Within the same range, absorption coefficients μ_a are in the range of 2.4 – 4.2 cm^{-1}, which is less than one-tenth of the corresponding scattering coefficients [38]. As a result, scattering, rather than absorption, dominate the light attenuation process in the NIR region.

Fig. 6 shows the calculated compound attenuation coefficient spectrum with different *W* over the selected NIR wavelength range from 750 to 840 nm to recover sO_2. When $W = 0$, the compound attenuation coefficient degraded to absorption coefficient [see Fig. 6(a)], from which the isosbesitic point at 797 nm can be clearly identified. However, as *W* increases from 0.01 to 0.1, the isosbesitic point shifted to a shorter wavelength [see Fig. 6(b)], and further moves out of the selected range [see Fig. 6(c) and (d)]. When *W* approaches 0.36, the shape of compound attenuation coefficient approaches the shape of scattering coefficient within the selected wavelength range, where the μ_{t_OxyB} spectrum is almost parallel to μ_{t_DeOxyB} spectrum [see Fig. 6(e)]. The same conclusion holds when using *W* greater than 0.36, as Fig. 6(e) shows the extreme case where $W = 1$.

For $W = 0.36$ used to extract sO_2 information, the least-squares fitting failed to converge due to the two linearly dependent inputs. The result indicates that OCT oximetry may only work when there is an obvious isosbestic point in the compound attenuation coefficients at the given packing factor. Though the wavelength we simulated are slightly shorter than the wavelength currently being used in the NIR OCT systems, they fall into the same absorption and scattering intensity range, and the two spectra have even less contrast in the longer wavelengths. Based on our data, visible light is clearly a better choice for OCT oximetry, unless more advanced signal processing techniques are developed.

REFERENCES

[1] T. W. Gardner *et al.*, "Diabetic retinopathy: More than meets the eye," *Surv. Ophthalmol.*, vol. 47, no. Suppl. 2, pp. S253–S262, 2002.

[2] D.-Y. Yu and S. J. Cringle, "Retinal degeneration and local oxygen metabolism," *Exp. Eye Res.*, vol. 80, no. 6, pp. 745–751, 2005.

[3] A. Harris *et al.*, "Measuring and interpreting ocular blood flow and metabolism in glaucoma," *Can. J. Ophthalmol.*, vol. 43, no. 3, pp. 328–336, 2008.

[4] N. D. Wangsa-Wirawan and R. A. Linsenmeier, "Retinal oxygen: Fundamental and clinical aspects," *Arch. Ophthalmol.*, vol. 121, no. 4, pp. 547–557, 2003.

[5] A. Harris *et al.*, "A review of methods for human retinal oximetry," *Ophthalmic Surg. Lasers Imaging*, vol. 34, no. 2, pp. 152–164, 2003.

[6] S. H. Hardarson and E. Stefánsson, "Retinal oxygen saturation is altered in diabetic retinopathy," *Brit. J. Ophthalmol.*, vol. 96, no. 4, pp. 560–563, 2012.

[7] O. B. Olafsdottir *et al.*, "Retinal oximetry in primary open-angle glaucoma," *Invest. Ophthalmol. Vis. Sci.*, vol. 52, no. 9, pp. 6409–6413, 2011.

[8] T. Eysteinsson *et al.*, "Retinal vessel oxygen saturation and vessel diameter in retinitis pigmentosa," *Acta Ophthalmol.*, vol. 92, no. 5, pp. 449–453, 2014.

[9] J. M. Beach *et al.*, "Oximetry of retinal vessels by dual-wavelength imaging: calibration and influence of pigmentation," *J. Appl. Physiol.*, vol. 86, no. 2, pp. 748–758, 1999.

[10] M. H. Smith *et al.*, "Effect of multiple light paths on retinal vessel oximetry," *Appl. Opt.*, vol. 39, no. 7, pp. 1183–1193, 2000.

[11] W. Liu *et al.*, "Accuracy of retinal oximetry: A Monte Carlo investigation," *J. Biomed. Opt.*, vol. 18, no. 6, pp. 0660031–06600310, 2013.

[12] H. F. Zhang *et al.*, "Functional photoacoustic microscopy for high-resolution and noninvasive in vivo imaging," *Nature Biotech.*, vol. 24, no. 7, pp. 848–851, 2006.

[13] J. Yi *et al.*, "Visible-light optical coherence tomography for retinal oximetry," *Opt. Lett.*, vol. 38, no. 11, pp. 1796–1798, 2013.

[14] L. Kagemann *et al.*, "Spectral oximetry assessed with high-speed ultra-high-resolution optical coherence tomography," *J. Biomed. Opt.*, vol. 12, no. 4, pp. 0412121–041218, 2007.

[15] D. J. Faber *et al.*, "Light absorption of (oxy-)hemoglobin assessed by spectroscopic optical coherence tomography," *Opt. Lett.*, vol. 28, no. 16, pp. 1436–1438, 2003.

[16] D. J. Faber *et al.*, "Toward assessment of blood oxygen saturation by spectroscopic optical coherence tomography," *Opt. Lett.*, vol. 30, no. 9, pp. 1015–1017, 2005.

[17] C.-W. Lu *et al.*, "Measurement of the hemoglobin oxygen saturation level with spectroscopic spectral-domain optical coherence tomography," *Opt. Lett.*, vol. 33, no. 5, pp. 416–418, 2008.

[18] F. E. Robles *et al.*, "Assessing hemoglobin concentration using spectroscopic optical coherence tomography for feasibility of tissue diagnostics," *Biomed. Opt. Exp.*, vol. 1, no. 1, pp. 310–317, 2010.

[19] J. Yi and X. Li, "Estimation of oxygen saturation from erythrocytes by high-resolution spectroscopic optical coherence tomography," *Opt. Lett.*, vol. 35, no. 12, pp. 2094–2096, 2010.

[20] F. E. Robles *et al.*, "Molecular imaging true-colour spectroscopic optical coherence tomography," *Nature Photon.*, vol. 5, no. 12, pp. 744–747, 2011.

[21] R. K. Wang, "Signal degradation by multiple scattering in optical coherence tomography of dense tissue: A Monte Carlo study towards optical clearing of biotissues," *Phys. Med. Biol.*, vol. 47, no. 13, pp. 2281–2299, 2002.

[22] J. M. Schmitt, "Optical coherence tomography (OCT): A review," *IEEE J. Sel. Topics Quantum*, vol. 5, no. 4, pp. 1205–1215, Jul./Aug. 1999.

[23] X. Zhang *et al.*, "Visible light optical coherence tomography for in vivo imaging the spectral contrasts of the retinal nerve fiber layer," *Proc. SPIE*, vol. 8213, pp. 82130H1–82130H7, 2012.

[24] L. V. Wang *et al.*, "MCML—Monte Carlo modeling of light transport in multi-layered tissues," *Comput. Methods Programs Biomed.*, vol. 47, no. 2, pp. 131–146, 1995.

[25] G. Yao and L. V. Wang, "Monte Carlo simulation of an optical coherence tomography signal in homogeneous turbid media," *Phys. Med. Biol.*, vol. 44, no. 9, pp. 2307–2320, 1999.

[26] A. Tycho *et al.*, "Derivation of a Monte Carlo method for modeling heterodyne detection in optical coherence tomography systems," *Appl. Opt.*, vol. 41, no. 31, pp. 6676–6691, 2002.

[27] M. Hammer *et al.*, "Light paths in retinal vessel oximetry," *IEEE Trans. Biomed. Eng.*, vol. 48, no. 5, pp. 592–598, May 2001.

[28] C. W. Oyster, *The Human Eye*. Sunderland, MA, USA: Sinauer Associates, 1999.

[29] C. E. Riva *et al.*, "Blood velocity and volumetric flow rate in human retinal vessels," *Invest. Ophthalmol. Vis. Sci.*, vol. 26, no. 8, pp. 1124–1132, 1985.

[30] M. Ritt and R. E. Schmieder, "Wall-to-lumen ratio of retinal arterioles as a tool to assess vascular changes," *Hypertension*, vol. 54, no. 2, pp. 384–387, 2009.

[31] M. Keijzer *et al.*, "Fluorescence spectroscopy of turbid media: Autofluorescence of the human aorta," *Appl. Opt.*, vol. 28, no. 20, pp. 4286–4292, 1989.

[32] M. Hammer *et al.*, "Optical properties of ocular fundus tissues-an in vitro study using the double-integrating-sphere technique and inverse Monte Carlo simulation," *Phys. Med. Biol.*, vol. 40, no. 6, pp. 963–978, 1995.

[33] S. Prahl. (1998, Mar.). Tabulated molar extinction coefficient for hemoglobin in water. [Online] Available: http://omlc.org/spectra/hemoglobin/summary.html

[34] A. Geirsdottir *et al.*, "Retinal vessel oxygen saturation in healthy individuals," *Invest. Ophthalmol. Vis. Sci.*, vol. 53, no. 9, pp. 5433–5442, 2012.

[35] D. J. Faber *et al.*, "Oxygen saturation-dependent absorption and scattering of blood," *Phys. Rev. Lett.*, vol. 93, no. 2, p. 028102, 2004.

[36] A. Roggan *et al.*, "Optical properties of circulating human blood in the wavelength range 400–2500 nm," *J. Biomed. Opt.*, vol. 4, no. 1, pp. 36–46, 1999.

[37] D. K. Sardar and L. B. Levy, "Optical properties of whole blood," *Laser. Med. Sci.*, vol. 13, no. 2, pp. 106–111, 1998.

[38] N. Bosschaart *et al.*, "A literature review and novel theoretical approach on the optical properties of whole blood," *Laser. Med. Sci.*, vol. 29, no. 2, pp. 453–479, 2013.

[39] Q. Lu *et al.*, "Monte Carlo modeling of optical coherence tomography imaging through turbid media," *Appl. Opt.*, vol. 43, no. 8, pp. 1628–1637, 2004.

[40] R. Leitgeb *et al.*, "Spectral measurement of absorption by spectroscopic frequency-domain optical coherence tomography," *Opt. Lett.*, vol. 25, no. 11, pp. 820–822, 2000.

[41] J. D. Rogers *et al.*, "Nonscalar elastic light scattering from continuous media in the Born approximation," *Opt. Lett.*, vol. 34, no. 12, pp. 1891–1893, 2009.

[42] J. Yi and V. Backman, "Imaging a full set of optical scattering properties of biological tissue by inverse spectroscopic optical coherence tomography," *Opt. Lett.*, vol. 37, no. 21, pp. 4443–4445, 2012.

[43] D. J. Faber *et al.*, "Hematocrit-dependence of the scattering coefficient of blood determined by optical coherence tomography," *Proc. SPIE*, vol. 6163, pp. 61630Y1–61630Y9, 2006.

[44] F. Sakai *et al.*, "Regional cerebral blood volume and hematocrit measured in normal human volunteers by single-photon emission computed tomography," *J. Cereb. Blood Flow Metab.*, vol. 5, no. 2, pp. 207–213, 1985.

[45] L. Pedersen *et al.*, "Quantitative measurement of changes in retinal vessel diameter in ocular fundus images," *Pattern Recogn. Lett.*, vol. 21, no. 13/14, pp. 1215–1223, 2000.

[46] J. S. Tiedeman *et al.*, "Retinal oxygen consumption during hyperglycemia in patients with diabetes without retinopathy," *Ophthalmology*, vol. 105, no. 1, pp. 31–36, 1998.

[47] J. Yi *et al.*, "Can OCT be sensitive to nanoscale structural alterations in biological tissue?," *Opt. Exp.*, vol. 21, no. 7, pp. 9043–9059, 2013.

Authors' photographs and biography not available at the time of publication.